



Suspended photonic crystal membranes in AlGaAs heterostructures for integrated multi-element optomechanics

Downloaded from: <https://research.chalmers.se>, 2025-12-10 01:21 UTC

Citation for the original published paper (version of record):

Kini, S., Elkhoully, K., Fitzgerald, J. et al (2020). Suspended photonic crystal membranes in AlGaAs heterostructures for integrated multi-element optomechanics. Applied Physics Letters, 116(26). <http://dx.doi.org/10.1063/5.0012667>

N.B. When citing this work, cite the original published paper.

Suspended photonic crystal membranes in AlGaAs heterostructures for integrated multi-element optomechanics ^{EP}

Cite as: Appl. Phys. Lett. **116**, 264001 (2020); <https://doi.org/10.1063/5.0012667>

Submitted: 03 May 2020 . Accepted: 10 June 2020 . Published Online: 29 June 2020

Sushanth Kini Manjeshwar ^{ID}, Karim Elkhoully ^{ID}, Jamie M. Fitzgerald ^{ID}, Martin Ekman, Yanchao Zhang, Fan Zhang, Shu Min Wang, Philippe Tassin, and Witlef Wieczorek ^{ID}

COLLECTIONS

Paper published as part of the special topic on [Hybrid Quantum Devices](#)

^{EP} This paper was selected as an Editor's Pick



View Online



Export Citation



CrossMark

ARTICLES YOU MAY BE INTERESTED IN

[First principle investigations on transport properties in porphyrin, hexaphyrin, and hexathia\[26 \$\pi\$ \]annulene molecular junction devices](#)

Applied Physics Letters **116**, 263301 (2020); <https://doi.org/10.1063/5.0004442>

[Surface control and MBE growth diagram for homoepitaxy on single-crystal AlN substrates](#)

Applied Physics Letters **116**, 262102 (2020); <https://doi.org/10.1063/5.0010813>

[Quantum confinement of coherent acoustic phonons in transferred single-crystalline bismuth nanofilms](#)

Applied Physics Letters **116**, 263101 (2020); <https://doi.org/10.1063/5.0007168>



HIDEN
ANALYTICAL


Instruments for Advanced Science

Gas Analysis



- dynamic measurement of reaction gas streams
- catalysis and thermal analysis
- molecular beam studies
- dissolved species probes
- fermentation, environmental and ecological studies

Surface Science



- UHV TPD
- SIMS
- end point detection in ion beam etch
- elemental imaging - surface mapping

Plasma Diagnostics



- plasma source characterization
- etch and deposition process reaction kinetic studies
- analysis of neutral and radical species

Vacuum Analysis



- partial pressure measurement and control of process gases
- reactive sputter process control
- vacuum diagnostics
- vacuum coating process monitoring

Contact Hiden Analytical for further details:
W www.HidenAnalytical.com
E info@hiden.co.uk

CLICK TO VIEW our product catalogue

Suspended photonic crystal membranes in AlGaAs heterostructures for integrated multi-element optomechanics

Cite as: Appl. Phys. Lett. **116**, 264001 (2020); doi: [10.1063/5.0012667](https://doi.org/10.1063/5.0012667)

Submitted: 3 May 2020 · Accepted: 10 June 2020 ·

Published Online: 29 June 2020



View Online



Export Citation



CrossMark

Sushanth Kini Manjeshwar,¹  Karim Elkhoully,^{1,a)}  Jamie M. Fitzgerald,²  Martin Ekman,² Yanchao Zhang,³ Fan Zhang,³ Shu Min Wang,¹ Philippe Tassin,² and Witlef Wieczorek^{1,b)} 

AFFILIATIONS

¹Department of Microtechnology and Nanoscience (MC2), Chalmers University of Technology, SE-412 96 Gothenburg, Sweden

²Department of Physics, Chalmers University of Technology, SE-412 96 Gothenburg, Sweden

³Zhejiang Supermat Sen-Ray Technology, No. 28, Middle Yunshan Road, 315400 Ningbo, China

Note: This paper is part of the Special Issue on Hybrid Quantum Devices

^{a)}Present address: IMEC, Kapeldreef 75, 3001 Leuven, Belgium.

^{b)}Author to whom correspondence should be addressed: witlef.wieczorek@chalmers.se

ABSTRACT

We present high-reflectivity mechanical resonators fabricated from AlGaAs heterostructures for use in free-space optical cavities operating in the telecom wavelength regime. The mechanical resonators are fabricated in slabs of GaAs and patterned with a photonic crystal to increase their out-of-plane reflectivity. Characterization of the mechanical modes reveals residual tensile stress in the GaAs device layer. This stress results in higher mechanical frequencies than in unstressed GaAs and can be used for strain engineering of mechanical dissipation. Simultaneously, we find that the finite waist of the incident optical beam leads to a dip in the reflectance spectrum. This feature originates from coupling to a guided resonance of the photonic crystal, an effect that must be taken into account when designing slabs of finite size. The single-layer and sub- μm -spaced double-layer slabs demonstrated here can be directly fabricated on top of a distributed Bragg reflector mirror in the same material platform. Such a platform opens a route for realizing integrated multi-element cavity optomechanical devices and optomechanical microcavities on chip.

© 2020 Author(s). All article content, except where otherwise noted, is licensed under a Creative Commons Attribution (CC BY) license (<http://creativecommons.org/licenses/by/4.0/>). <https://doi.org/10.1063/5.0012667>

Cavity optomechanical devices explore the interaction between light and mechanical resonators in a cavity¹ and rely on strongly coupled, high-quality optical and mechanical resonators. When several independent mechanical resonators are coupled to a single cavity field, one is in the realm of multi-element optomechanics,^{2,3} which has been proposed as a route to reach the elusive single-photon strong optomechanical coupling regime.^{4,5} Recent experiments along these lines^{6–9} have used SiN membranes placed in free-space optical cavities but require precise alignment of their tilt angle and position and, additionally, a uniformity of the mechanical and optical properties of individual membranes.

Using III–V heterostructures such as AlGaAs would allow for the realization of a multi-element cavity optomechanical system in a fully integrated approach.^{10,11} A heterostructure can integrate one of the cavity mirrors via a distributed Bragg reflector together with an array

of near-uniform mechanical resonators on a single wafer^{10–12} and can even be combined with micro-mirrors on an independent chip.¹³ In particular, the III–V materials system has already been used to realize (opto)mechanical systems in, e.g., (Al)GaAs^{14–25} or In(Ga)P.^{11,26–28} These crystalline materials have been shown to be of high optical and mechanical quality^{11,20,24} as required for cavity optomechanics. Further device functionalization based on the piezoelectricity of III–V materials or by embedding quantum emitters can lead to versatile nano-electro-optomechanical systems.³⁰

In this Letter, we demonstrate the fabrication of single- and double-layer membranes in AlGaAs heterostructures³¹ and present a comprehensive characterization of single-layer high-reflectivity mechanical resonators. The mechanical resonators are fabricated in 100 nm-thin GaAs membranes, which are grown on top of sacrificial AlGaAs layers. This allows us to fabricate double-layer membranes

with sub- μm spacing, which is crucial for reaching high coupling strengths in multi-element optomechanics.^{2,3} We engineer mechanical resonators of free-free-type geometry^{11,17} and characterize their mechanical properties. We demonstrate control over their out-of-plane optical reflectivity in the telecom wavelength regime by patterning a photonic crystal (PhC) into the GaAs membranes,³² as has been demonstrated in optomechanics^{27,33–37} and optical communication technologies.^{38,39} Our devices constitute a significant step toward the realization of an array of near-uniform mechanical resonators integrated in a free-space, fully chip-based cavity optomechanical device.

The mechanically compliant PhC slabs are fabricated in an AlGaAs heterostructure that is epitaxially grown on a GaAs substrate using molecular-beam epitaxy. We fabricated devices from two different wafers. The heterostructure of the first wafer is used for single-layer mechanical resonators [Fig. 1(a)]. It consists of a 100 nm-thick GaAs device layer grown on top of a 4 μm -thick $\text{Al}_{0.65}\text{Ga}_{0.35}\text{As}$ sacrificial layer. The AlGaAs layer exhibited a large peak-to-peak surface height variation of 15 nm, which is partially smoothed by the top GaAs layer to 10 nm, yielding an average GaAs layer thickness of 89 nm inferred from transmission electron microscopy (TEM) and ellipsometry measurements.

The second wafer is designed for fabricating sub- μm spaced, double-layer GaAs mechanical devices [Fig. 1(b)], each of 100 nm thickness on top of a 729 nm $\text{Al}_{0.625}\text{Ga}_{0.375}\text{As}$ sacrificial layer, which defines the spacing between the two GaAs slabs. These AlGaAs layers were grown with growth interruption,⁴⁰ yielding a surface height variation and roughness smaller than 1 nm and 0.2 nm, respectively. We used standard AlGaAs heterostructure^{38,41} microfabrication techniques to define the patterned mechanical resonators and their release (see the [supplementary material](#) for details).

The mechanical resonators are engineered with a free-free-type geometry,¹⁷ where the suspended slab is of rectangular shape and held by four tethers at the nodes of the free-free oscillation mode¹⁸ [see Fig. 2(b)]. First, we characterized the mechanical properties of the slabs, focusing on the mode shapes and corresponding eigenfrequencies and quality factors. To this end, we detected the out-of-plane

displacement of the slab via optical homodyne interferometry at room temperature in a high vacuum ($\sim 5 \times 10^{-5}$ mbar)—for details of the setup, see the [supplementary material](#). Figure 2(a) shows a typical displacement noise power spectrum of a PhC slab with a size of $50 \times 50 \times 0.1 \mu\text{m}^3$. The fundamental mode lies at 80 kHz and the free-free mode at 178 kHz. Mechanical mode tomography⁴² enabled us to compare the measured mode shape to finite element modeling (FEM) simulations⁴³ [see Fig. 2(b)]. We find good agreement between experimental and FEM data when accounting for a tensile stress of 10 MPa in the GaAs layer.

We attribute the residual tensile stress to a mismatch between the lattice constants of the AlGaAs sacrificial and GaAs device epilayers. AlGaAs grown on the GaAs substrate relaxes to its native lattice constant if the layer thickness exceeds the critical thickness of 0.33 μm or 30 μm , according to Refs. 44 or 45, respectively (see also the [supplementary material](#)). These predictions differ by two orders of magnitude such that the AlGaAs layer can be in a state between fully relaxed and fully strained, depending on the model used.^{44,45} The GaAs device layer is thinner than its critical thickness and, thus, adapts to the lattice constant of the AlGaAs layer in any case. Then, the GaAs device layer can exhibit a tensile stress of between 0 and 77.5 MPa.

In Fig. 3(a), we examine the effect of tensile stress in the GaAs device layer on the eigenfrequencies of the suspended slab. We observe that the frequencies increase with stress and find a match between data and FEM for a stress around 10 MPa. Upon removal of the sacrificial AlGaAs layer, an anisotropic stress distribution develops in the suspended GaAs slab, as shown in Fig. 2(c). We also observe buckling of the slabs⁴⁶ and a static deformation.⁴⁷ For example, Fig. 1(c) shows a slab with 280 nm buckling and a static deformation of 400 nm along the direction indicated by the red line. We conclude that the GaAs layer exhibits residual tensile stress induced by the underlying AlGaAs layer, as was observed in other GaAs on AlGaAs resonators.^{20,46,47}

Spatial variations of the resonator geometry⁴⁶ or defect-driven material anisotropy²⁸ also influence the mechanical properties. While analysis of the latter is beyond the scope of our work, the former can be caused by growth-related thickness variation or microfabrication-induced changes. Geometry variations influence the mode-dependent oscillating mass of the resonator and, thus, its eigenfrequencies.

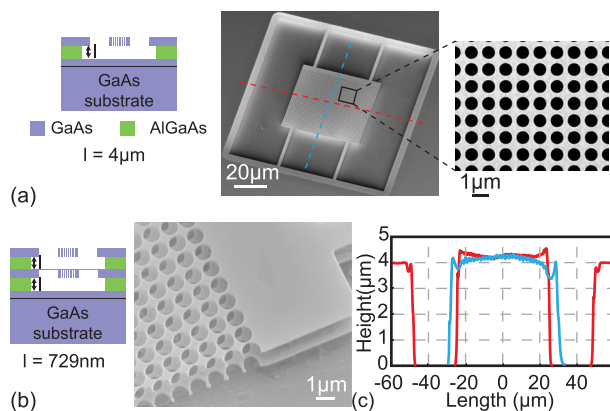


FIG. 1. Free-free-type mechanical resonators fabricated in AlGaAs heterostructures. (a) Schematic of the AlGaAs heterostructure and scanning electron microscopy (SEM) images of a single-layer free-free-type mechanical resonator structured as a photonic crystal (PhC) membrane. (b) Schematic and SEM image of a double-layer PhC device. (c) Height profile of the device from (a).

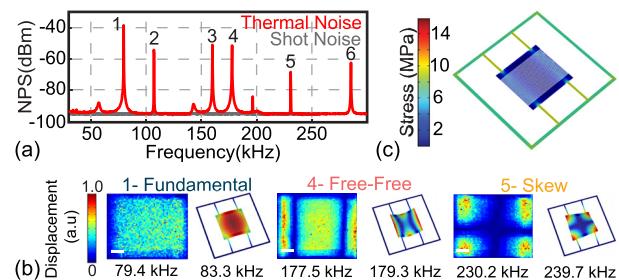


FIG. 2. Characterization of mechanical modes of a free-free-type PhC slab. (a) Noise power spectrum (NPS) of the thermally driven mechanical motion (red) with mechanical modes labeled 1–6. (b) Mechanical-mode tomography of the same device along with FEM-simulated mode shapes and their frequencies. Scale bar: 10 μm . Note that the device boundary inferred from mode tomography is largely determined by the rectangular $50 \times 38 \mu\text{m}^2$ PhC area that reflects more light than the non-patterned part and, thus, leads to an apparent deviation from the square shape of the slab. (c) FEM-simulated von Mises stress distribution of the device.

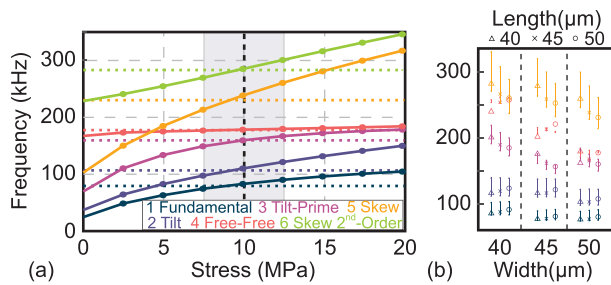


FIG. 3. (a) FEM simulation results for mechanical frequencies of a $50 \times 50 \mu\text{m}^2$ PhC patterned device with varying tensile stresses in a 105 nm-thick GaAs layer (lines are guides to the eye). The dotted horizontal lines show the measured frequencies from Fig. 2(a). (b) Measured frequencies for patterned devices of different dimensions. The bars around each data point denote the FEM-simulated frequency range corresponding to the stress range marked by the shaded region in (a).

We account for the geometry of the devices in FEM with the simplifying assumption of a constant GaAs layer thickness. Figure 3(b) shows frequencies for devices of various slab lengths and widths. For a layer thickness of 105 nm assumed in the FEM, we find good agreement between measured and FEM-simulated frequencies (see the [supplementary material](#) for detailed simulation results). We attribute the thickness difference of 15 nm between FEM and the TEM/ellipsometry measurements to the assumption in the FEM that the GaAs layer exhibits a constant thickness, which simplifies modeling, but neglects spatial mass variations of the slab. Overall, residual tensile stress in the GaAs layer and the simplifying assumption of its constant thickness yield a reasonable explanation for the observed mechanical frequencies of the suspended PhC slabs.

The mechanical quality factor, Q , is an important figure of merit for (opto)mechanical devices. We find that devices fabricated from the first wafer have quality factors just below 10^5 and similar devices from the second wafer reach 3×10^5 (see the [supplementary material](#) for all data), which is about a factor of 10 larger (4 smaller) than Refs. 18 and 47 (Ref. 20). We do not observe any systematic discrepancy between the Q values of patterned and unpatterned devices. We expect an increase in Q by at least an order of magnitude when using samples with smoother surfaces,²⁹ operating at lower temperatures,^{24,47} and using strain engineering.

The unpatterned membrane has an out-of-plane optical reflectance of 69% at a free-space wavelength of 1550 nm, which is too low for reaching single-photon strong coupling in a multi-element optomechanical device.^{2,3} By patterning the membranes as PhC with air holes arranged in a square lattice,^{27,32–34,36} we can engineer a reflectance between 0% and 100% (Fig. 4), which we calculated using rigorous coupled wave analysis, e.g., via the S4 package.⁵⁰ To demonstrate this capability, we fabricated devices aiming at reflectances of (i) 99%, (ii) 75%, and (iii) 50% at 1550 nm.

We focus on device (i) in Fig. 5 and discuss devices (ii) and (iii) in the [supplementary material](#) along with a description of the optical setup used to measure reflectance.⁵¹ In Fig. 5(a), we observe a maximum of the reflectance around 1510 nm, away from the designed maximum at 1550 nm. We reproduce this shift for a slab with a thickness of 87.5 nm in the PhC simulation (instead of the assumed 100 nm), which closely matches the thickness of 89 nm inferred from the TEM and ellipsometry measurements.

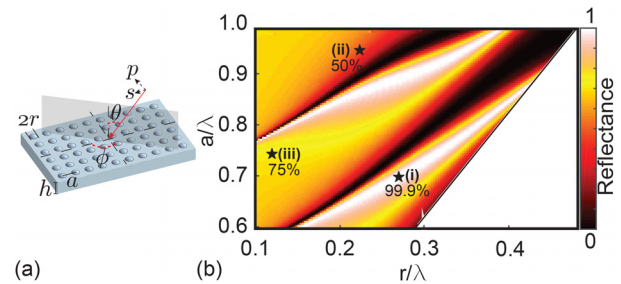


FIG. 4. (a) Schematic of a PhC slab of thickness h with a square PhC of lattice constant a and hole radius r . A plane wave is incident at polar angle θ and azimuthal angle ϕ with polarization components s and p . (b) Reflectance map for a $\lambda = 1550$ nm plane wave at normal incidence on a $h = 100$ nm GaAs PhC slab for varying r and a . The stars mark PhC patterns with (i) $a = 1081$ nm, $r = 418$ nm ($R > 99\%$), (ii) $a = 1452.8$ nm, $r = 318.8$ nm ($R = 50\%$), and (iii) $a = 1162.8$ nm, $r = 159.18$ nm ($R = 75\%$).

Notably, the reflectance spectrum in Fig. 5(a) shows a pronounced dip at 1581 nm. This dip can only be reproduced when taking into account the finite waist of the incident beam. To this end, we model the incident Gaussian beam as a weighted sum of plane waves

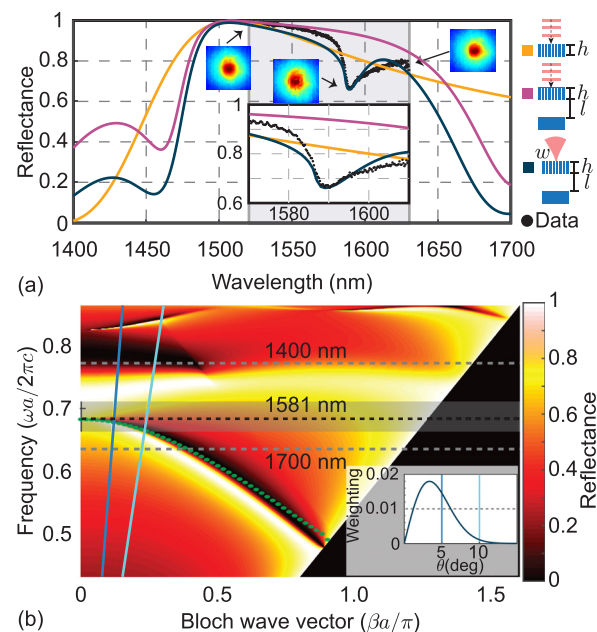


FIG. 5. (a) Reflectance spectra of a suspended GaAs PhC membrane of thickness $h = 87.5$ nm and air-gap $l = 4.3 \mu\text{m}$. The data (black) are compared to simulated spectra for a plane wave/Gaussian beam of waist $4.2 \mu\text{m}$ incident on the PhC slab (orange)/(–) or on the slab on top of a GaAs substrate (purple)/(blue). The gray region marks the measurement range. The insets show transverse mode patterns measured in reflection. (b) Reflectance map of a PhC membrane for an incident plane wave of wave vector $\beta = \frac{2\pi}{\lambda} \sin(\theta)$ and frequency ω . The green dots show the dispersion of the guided resonance for an s-polarized wave. The inset shows the weighting factor of plane waves used for representing a Gaussian beam of waist $4.2 \mu\text{m}$. The blue lines mark the same angles of incidence in the inset and main panel.

incident at polar angle θ and azimuthal angle ϕ [Figs. 4(a) and inset 5(b)] (see Refs. 37 and 52 and the supplementary material). The dip results from coupling of plane waves at oblique incidence to a guided resonance of the PhC. This can be best illustrated with the reflectance map of the PhC slab shown in Fig. 5(b). The dispersion relation of the guided resonance at 1581 nm at wave vector $\beta = 0$ shows a decrease in frequency with an increase in β . Hence, the guided resonance appears at longer wavelengths for light impinging under oblique incidence. As a Gaussian beam is formed by the weighted sum of many plane waves, a reflectance dip of finite spectral width is formed.

In Fig. 6(a), we examine the effect of varying waist on reflectance. For larger waists, the dip in the spectrum narrows. The reason for this behavior is that larger waists are represented by plane waves with weighting factors that favor less oblique contributions, and thus, less dispersion of the guided resonance is collected. Furthermore, a larger waist reaches a larger reflectance,³⁷ as seen in the inset of Fig. 6(a). In our measurements in Fig. 6(b), we observe that the dip width indeed decreases with increasing waist. However, in contrast to our prediction, we observe an overall drop in reflectance with larger waists. We attribute this drop to clipping loss due to the finite size of the slab and to diffraction loss of the guided resonance at the boundaries of the slab.⁵³

Finally, we study the dependence of reflectance on parameters of the PhC device. Figure 6(c) shows that the dip shifts to shorter wavelengths upon increasing the radius of the PhC holes. This shift is expected as the patterning determines the PhC mode structure.

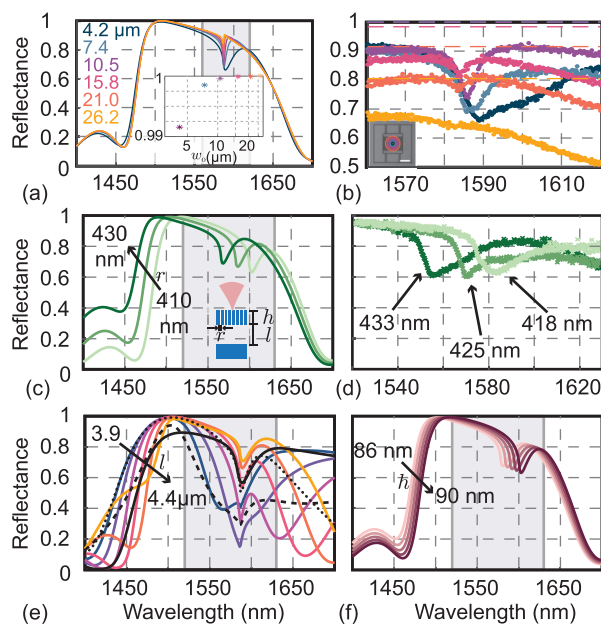


FIG. 6. (a) Reflectance spectra of a Gaussian beam of varying waist size incident on an infinite PhC slab on top of a substrate. The inset shows the maximal achievable reflectance for a given waist. (b) Measured spectra for different waist sizes. The horizontal dashed lines represent the expected clipping loss (see the inset). Scale bar: 25 μm . (c) Calculated and (d) measured reflectance spectra when varying the PhC hole radius r . The calculated reflectance spectrum when varying (e) the air-gap spacing l (with black solid, dashed, and dotted lines representing $l = 0.5, 0.75$, and $1 \mu\text{m}$, respectively) and (f) slab thickness h .

We illustrate this behavior with three devices in Fig. 6(d). Figure 6(e) shows the dependence on the air-gap l . We observe that the position of the dip remains constant, as expected since the mode structure of the PhC slab is not influenced by l . However, the reflectance at the dip depends strongly on l . This is the result of a spectral shift of the Fabry-Pérot resonance formed by the slab and substrate through the dip. Figure 6(f) shows the dependence on slab thickness h . We observe that the dip shifts to longer wavelengths with increasing h , with a strong shift of 4.5 nm in wavelength per nm change in thickness. Hence, a precise knowledge of the slab thickness is required to engineer the position of the dip accurately.

To conclude, we have demonstrated the engineering of suspended PhC slabs in GaAs with mechanical resonance frequencies above 50 kHz, quality factors as high as 3×10^5 at room temperature, a maximal $Q \times f$ product of 10^{11} Hz, and a controllable out-of-plane reflectance at telecom wavelengths.^{32,34,35} The GaAs device layer exhibited residual tensile stress, which can be favorably used for strain engineering to reduce mechanical dissipation as demonstrated, e.g., with SiN^{34,48,49,54,55} or III-V-based resonators.^{11,15,28,56} A dip in the reflectance spectrum^{35,37,52} originating from coupling to a guided resonance in the PhC was observed. Hence, PhC devices of finite size must be carefully engineered to have this dip outside of a desired high-reflectivity region.

The mechanical resonator slabs in GaAs presented in this Letter can be engineered into arrays of high-reflectivity mechanical resonators of precise, epitaxially defined thickness and spacing using AlGaAs heterostructures integrated on top of a distributed Bragg reflector.^{10,47} Such an integrated system presents exciting perspectives for realizing free-space and fully chip-based multi-element cavity optomechanical systems,^{2,6–9} optomechanical microcavities,¹⁰ or frequency-dependent mirrors in optical cavities.^{57,58}

See the supplementary material for detailed descriptions of device fabrication, experimental setups, FEM simulations, modeling of PhC reflectance, and further data.

We acknowledge fruitful discussions with Claus Gärtner, Garrett D. Cole, and Martí Gutierrez Latorre. This work was supported by Chalmers' Excellence Initiative Nano, the Knut and Alice Wallenberg Foundation, the Swedish Research Council, and the QuanterA project C'MON-QSENS!. Samples were fabricated in the Myfab Nanofabrication Laboratory at Chalmers and analyzed in the Chalmers Materials Analysis Laboratory. Simulations were performed on resources provided by the Swedish National Infrastructure for Computing at C3SE.

DATA AVAILABILITY

The data that support the findings of this study are openly available in [zenodo.org] at <https://doi.org/10.5281/zenodo.3783499>.

REFERENCES

- ¹M. Aspelmeyer, T. J. Kippenberg, and F. Marquardt, *Rev. Mod. Phys.* **86**, 1391 (2014).
- ²A. Xuereb, C. Genes, and A. Dantan, *Phys. Rev. Lett.* **109**, 223601 (2012).
- ³A. Xuereb, C. Genes, and A. Dantan, *Phys. Rev. A* **88**, 053803 (2013).
- ⁴P. Rabl, *Phys. Rev. Lett.* **107**, 063601 (2011).
- ⁵A. Nunnenkamp, K. Børkje, and S. M. Girvin, *Phys. Rev. Lett.* **107**, 063602 (2011).

- ⁶B. Nair, A. Naesby, and A. Dantan, *Opt. Lett.* **42**, 1341 (2017).
- ⁷P. Piergentili, L. Catalini, M. Bawaj, S. Zippilli, N. Malossi, R. Natali, D. Vitali, and G. D. Giuseppe, *New J. Phys.* **20**, 083024 (2018).
- ⁸C. Gärtner, J. P. Moura, W. Haaxman, R. A. Norte, and S. Gröblacher, *Nano Lett.* **18**, 7171 (2018).
- ⁹X. Wei, J. Sheng, C. Yang, Y. Wu, and H. Wu, *Phys. Rev. A* **99**, 023851 (2019).
- ¹⁰M. R. Vanner, I. Pikovski, G. D. Cole, M. S. Kim, C. Brukner, K. Hammerer, G. J. Milburn, and M. Aspelmeyer, *Proc. Natl. Acad. Sci.* **108**, 16182 (2011).
- ¹¹G. D. Cole, P.-L. Yu, C. Gärtner, K. Siquans, R. Moghadas Nia, J. Schmölle, J. Hoelscher-Obermaier, T. P. Purdy, W. Wiecek, C. A. Regal, and M. Aspelmeyer, *Appl. Phys. Lett.* **104**, 201908 (2014).
- ¹²Y.-G. Roh, T. Tanabe, A. Shinya, H. Taniyama, E. Kuramochi, S. Matsuo, T. Sato, and M. Notomi, *Phys. Rev. B* **81**, 121101 (2010).
- ¹³G. Wachter, S. Kuhn, S. Minniberger, C. Salter, P. Asenbaum, J. Millen, M. Schneider, J. Schalko, U. Schmid, A. Felgner, D. Hüser, M. Arndt, and M. Trupke, *Light Sci. Appl.* **8**, 37 (2019).
- ¹⁴H. Yamaguchi, K. Kato, Y. Nakai, K. Onomitsu, S. Warisawa, and S. Ishihara, *Appl. Phys. Lett.* **92**, 251913 (2008).
- ¹⁵T. Watanabe, K. Onomitsu, and H. Yamaguchi, *Appl. Phys. Express* **3**, 065201 (2010).
- ¹⁶L. Ding, C. Baker, P. Senellart, A. Lemaitre, S. Ducci, G. Leo, and I. Favero, *Phys. Rev. Lett.* **105**, 263903 (2010).
- ¹⁷G. D. Cole, I. Wilson-Rae, M. R. Vanner, S. Gröblacher, J. Pohl, M. Zorn, M. Weyers, A. Peters, and M. Aspelmeyer, in *Proceedings of the IEEE MEMS* (2010), p. 847.
- ¹⁸G. D. Cole, I. Wilson-Rae, K. Werbach, M. R. Vanner, and M. Aspelmeyer, *Nat. Commun.* **2**, 231 (2011).
- ¹⁹H. Okamoto, D. Ito, K. Onomitsu, H. Sanada, H. Gotoh, T. Sogawa, and H. Yamaguchi, *Phys. Rev. Lett.* **106**, 036801 (2011).
- ²⁰J. Liu, K. Usami, A. Naesby, T. Bagci, E. S. Polzik, P. Lodahl, and S. Stobbe, *Appl. Phys. Lett.* **99**, 243102 (2011).
- ²¹K. Usami, A. Naesby, T. Bagci, B. Melholt Nielsen, J. Liu, S. Stobbe, P. Lodahl, and E. S. Polzik, *Nat. Phys.* **8**, 168 (2012).
- ²²L. Midolo and A. Fiore, *IEEE J. Quantum Electron.* **50**, 404 (2014).
- ²³H. Yamaguchi, *Semicond. Sci. Technol.* **32**, 103003 (2017).
- ²⁴M. Hamoumi, P. Allain, W. Hease, E. Gil-Santos, L. Morgenroth, B. Gérard, A. Lemaitre, G. Leo, and I. Favero, *Phys. Rev. Lett.* **120**, 223601 (2018).
- ²⁵M. Cotrufo, L. Midolo, Z. Zobenica, M. Petruzzella, F. W. M. van Otten, and A. Fiore, *Phys. Rev. B* **97**, 115304 (2018).
- ²⁶T. Antoni, A. G. Kuhn, T. Briant, P.-F. Cohadon, A. Heidmann, R. Braive, A. Beveratos, I. Abram, L. L. Gratiot, I. Sagnes, and I. Robert-Philip, *Opt. Lett.* **36**, 3434 (2011).
- ²⁷K. Makles, T. Antoni, A. G. Kuhn, S. Deléglise, T. Briant, P.-F. Cohadon, R. Braive, G. Beaudoin, L. Pinard, C. Michel, V. Dolique, R. Flaminio, G. Cagnoli, I. Robert-Philip, and A. Heidmann, *Opt. Lett.* **40**, 174 (2015).
- ²⁸M. Bückle, V. C. Hauber, G. D. Cole, C. Gärtner, U. Zeimer, J. Grenzer, and E. M. Weig, *Appl. Phys. Lett.* **113**, 201903 (2018).
- ²⁹G. D. Cole, W. Zhang, B. J. Bjork, D. Follman, P. Heu, C. Deutsch, L. Sonderhouse, J. Robinson, C. Franz, A. Alexandrovski, M. Notcutt, O. H. Heckl, J. Ye, and M. Aspelmeyer, *Optica* **3**, 647 (2016).
- ³⁰L. Midolo, A. Schliesser, and A. Fiore, *Nat. Nanotechnol.* **13**, 11 (2018).
- ³¹M. J. Manfra, *Annu. Rev. Condens. Matter Phys.* **5**, 347 (2014).
- ³²S. Fan and J. D. Joannopoulos, *Phys. Rev. B* **65**, 235112 (2002).
- ³³C. H. Bui, J. Zheng, S. W. Hoch, L. Y. T. Lee, J. G. E. Harris, and C. W. Wong, *Appl. Phys. Lett.* **100**, 021110 (2012).
- ³⁴R. A. Norte, J. P. Moura, and S. Gröblacher, *Phys. Rev. Lett.* **116**, 147202 (2016).
- ³⁵S. Bernard, C. Reinhardt, V. Dumont, Y.-A. Peter, and J. C. Sankey, *Opt. Lett.* **41**, 5624 (2016).
- ³⁶X. Chen, C. Chardin, K. Makles, C. Caër, S. Chua, R. Braive, I. Robert-Philip, T. Briant, P. F. Cohadon, A. Heidmann, T. Jacqmin, and S. Deléglise, *Light* **6**, e16190 (2017).
- ³⁷J. P. Moura, R. A. Norte, J. Guo, C. Schäfermeier, and S. Gröblacher, *Opt. Express* **26**, 1895 (2018).
- ³⁸T. Stomeo, M. Grande, G. Raino, A. Passaseo, A. D'Orazio, R. Cingolani, A. Locatelli, D. Modotto, C. De Angelis, and M. D. Vittorio, *Opt. Lett.* **35**, 411 (2010).
- ³⁹W. Zhou, D. Zhao, Y.-C. Shuai, H. Yang, S. Chuwongin, A. Chadha, J.-H. Seo, K. X. Wang, V. Liu, Z. Ma, and S. Fan, *Prog. Quantum Electron.* **38**(1), 1 (2014).
- ⁴⁰J. Sweet, B. C. Richards, J. D. Olitzky, J. Hendrickson, G. Khitrova, H. M. Gibbs, D. Litvinov, D. Gerthsen, D. Z. Hu, D. M. Schaadt, M. Wegener, U. Khankhoje, and A. Scherer, *Photonics Nanostruct.-Fundam. Appl.* **8**(1), 1 (2010).
- ⁴¹L. Midolo, T. Pregnolato, G. Kiršanskė, and S. Stobbe, *Nanotechnology* **26**, 484002 (2015).
- ⁴²A. Barg, Y. Tsaturyan, E. Belhage, W. H. P. Nielsen, C. B. Møller, and A. Schliesser, *Appl. Phys. B* **123**, 8 (2017).
- ⁴³COMSOL AB, Stockholm, Sweden, see www.comsol.com "COMSOL Multiphysics," 2019.
- ⁴⁴J. W. Matthews, S. Mader, and T. B. Light, *J. Appl. Phys.* **41**, 3800 (1970).
- ⁴⁵R. People and J. C. Bean, *Appl. Phys. Lett.* **47**, 322 (1985).
- ⁴⁶A. A. Shevryin, A. G. Pogosev, M. V. Budantsev, A. K. Bakarov, A. I. Toropov, S. V. Ishutkin, E. V. Shesterikov, A. S. Kozhukhov, S. S. Kosolobov, and T. A. Gavrilova, *Appl. Phys. Lett.* **101**, 241916 (2012).
- ⁴⁷A. Barg, L. Midolo, G. Kiršanskė, P. Tighineanu, T. Pregnolato, A. İmamoğlu, P. Lodahl, A. Schliesser, S. Stobbe, and E. S. Polzik, *Phys. Rev. B* **98**, 155316 (2018).
- ⁴⁸Y. Tsaturyan, A. Barg, E. S. Polzik, and A. Schliesser, *Nat. Nanotechnol.* **12**, 776 (2017).
- ⁴⁹A. H. Ghadimi, S. A. Fedorov, N. J. Engelsen, M. J. Beryhi, R. Schilling, D. J. Wilson, and T. J. Kippenberg, *Science* **360**, 764 (2018).
- ⁵⁰V. Liu and S. Fan, *Comput. Phys. Commun.* **183**, 2233 (2012).
- ⁵¹K. Rivoire, A. Faraon, and J. Vuckovic, *Appl. Phys. Lett.* **93**, 063103 (2008).
- ⁵²A. Singh Chadha, D. Zhao, S. Chuwongin, Z. Ma, and W. Zhou, *Appl. Phys. Lett.* **103**, 211107 (2013).
- ⁵³J. O. Grepstad, M. M. Greve, B. Holst, I.-R. Johansen, O. Solgaard, and A. Sudbø, *Opt. Express* **21**, 23640 (2013).
- ⁵⁴S. S. Verbridge, J. M. Parpia, R. B. Reichenbach, L. M. Bellan, and H. G. Craighead, *J. Appl. Phys.* **99**, 124304 (2006).
- ⁵⁵C. Reinhardt, T. Müller, A. Bourassa, and J. C. Sankey, *Phys. Rev. X* **6**, 021001 (2016).
- ⁵⁶K. Onomitsu, M. Mitsuhashi, H. Yamamoto, and H. Yamaguchi, *Appl. Phys. Express* **6**, 111201 (2013).
- ⁵⁷A. Naesby and A. Dantan, *Opt. Express* **26**, 29886 (2018).
- ⁵⁸O. Černotík, A. Dantan, and C. Genes, *Phys. Rev. Lett.* **122**, 243601 (2019).